Title: Inference of Direct and Multistep Effective Connectivities from Functional Connectivity of the Brain and of Relationships to Cortical Geometry

Author: Grishma Mehta-Pandejee P.A. Robinson James A. Henderson K.M. Aquino Somwrita Sarkar

PII: S0165-0270(17)30069-9
DOI: http://dx.doi.org/doi:10.1016/j.jneumeth.2017.03.014
Reference: NSM 7700

To appear in: *Journal of Neuroscience Methods*

Received date: 1-11-2016
Revised date: 15-3-2017
Accepted date: 18-3-2017

Please cite this article as: Grishma Mehta-Pandejee, P.A. Robinson, James A. Henderson, K.M. Aquino, Somwrita Sarkar, Inference of Direct and Multistep Effective Connectivities from Functional Connectivity of the Brain and of Relationships to Cortical Geometry, *<![CDATA[Journal of Neuroscience Methods]]>* (2017), http://dx.doi.org/10.1016/j.jneumeth.2017.03.014

Title: Inference of Direct and Multistep Effective Connectivities from Functional Connectivity of the Brain and of Relationships to Cortical Geometry

Article Type: Research Paper

Authors and Affiliation:

Grishma Mehta-Pandejee[a,b,*], P. A. Robinson[a,b], James A. Henderson[a,b,c], K. M. Aquino[a,b,e], Somwrita Sarkar[b,d]

[a]School of Physics, The University of Sydney, Sydney, New South Wales 2006, Australia
[b]Center of Excellence for Integrative Brain Function, The University of Sydney, New South Wales 2006, Australia
[c]School of Information Technology and Electrical Engineering, University of Queensland, St Lucia, Queensland 4072, Australia
[d]Design Lab, University of Sydney, Sydney, New South Wales 2006, Australia
[e]Sir Peter Mansfield Imaging Center, University of Nottingham, Nottingham, NG7 2RD, UK, EU

[*]**Corresponding author:**

Grishma Mehta-Pandejee

Present/permanent address:

School of Physics, A28,
The University of Sydney,
Camperdown,
NSW 2006
Phone: (++61) 290367274
Email: grishma.pandejee@sydney.edu.au

Highlights

- Neural Field Theory (NFT) can yield effective connectivity from functional connectivity.
- Effective and functional connectivity are related to cortical geometry.
- Norm-minimization is a useful method to infer effective connectivity.

Inference of Direct and Multistep Effective Connectivities from Functional Connectivity of the Brain and of Relationships to Cortical Geometry

Grishma Mehta-Pandejee[a,b,*], P. A. Robinson[a,b], James A. Henderson[a,b,c], K. M. Aquino[a,b,e], Somwrita Sarkar[b,d]

[a] *School of Physics, The University of Sydney, Sydney, New South Wales 2006, Australia*
[b] *Center of Excellence for Integrative Brain Function, The University of Sydney, New South Wales 2006, Australia*
[c] *School of Information Technology and Electrical Engineering, University of Queensland, St Lucia, Queensland 4072, Australia*
[d] *Design Lab, University of Sydney, Sydney, New South Wales 2006, Australia*
[e] *Sir Peter Mansfield Imaging Center, University of Nottingham, Nottingham, NG7 2RD, UK, EU*

Abstract

Background : The problem of inferring effective brain connectivity from functional connectivity is under active investigation, and connectivity via multistep paths is poorly understood.

New method : A method is presented to calculate the direct effective connection matrix (deCM), which embodies direct connection strengths between brain regions, from functional CMs (fCMs) by minimizing the difference between an experimental fCM and one calculated via neural field theory from an ansatz deCM based on an experimental anatomical CM.

Results : The best match between fCMs occurs close to a critical point, consistent with independent published stability estimates. Residual mismatch between fCMs is identified to be largely due to interhemispheric connections that are poorly estimated in an initial ansatz deCM due to experimental limitations; improved ansatzes substantially reduce the mismatch and enable inter-

*Corresponding author
Email address: grishma.pandejee@sydney.edu.au (Grishma Mehta-Pandejee)

hemispheric connections to be estimated. Various levels of significant multistep connections are then imaged via the neural field theory (NFT) result that these correspond to powers of the deCM; these are shown to be predictable from geometric distances between regions.

Comparison with existing methods : This method gives insight into direct and multistep effective connectivity from fCMs and relating to physiology and brain geometry. This contrasts with other methods, which progressively adjust connections without an overarching physiologically based framework to deal with multistep or poorly estimated connections.

Conclusions : deCMs can be usefully estimated using this method and the results enable multistep connections to be investigated systematically.

Keywords: Functional connectivity, Effective connectivity, Anatomical connectivity, Neural field theory, Cortical geometry, Multistep connections, Norm-minimization, Global mode removal.

1. Introduction

The need to understand how the brain perform tasks rapidly, processes inputs, develops, responds to damage, and changes its connectivity as a result of lesions, has led to enormous interest in identifying the interrelationships between function and anatomy of the brain (Friston, 2011; Bullmore and Sporns, 2009; Rubinov et al., 2009; Sporns et al., 2004, 2000; Kaiser et al., 2010; Honey et al., 2007; Robinson et al., 2009; Henderson and Robinson, 2011; Sporns, 2010; Honey et al., 2010; Rubinov et al., 2011; Bassett et al., 2006; Gray and Robinson, 2009; Gray et al., 2009; Kitzbichler et al., 2009; Sporns et al., 2005; Beggs and Plenz, 2003; Stam and de Bruin, 2004; Linkenkaer-Hansen et al., 2001; Albert and Barabási, 2002; Barthélemy, 2011; Galán, 2008; Honey et al., 2009). Experiments and analysis on the "resting" (i.e., free of conscious processing and

experimental tasks) human brain show that the functional connectivity is supported by anatomical connectivity (Hagmann et al., 2008; Honey et al., 2009; Deco et al., 2014; Damoiseaux et al., 2006).

Connectivity between brain regions is often expressed via connection matrices (CMs), where rows and columns of the matrix represent brain regions (Friston, 2011; Bullmore and Sporns, 2009; Sporns, 2010) and entries represent the connections between them. Anatomical connection matrices (aCMs, sometimes termed structural connection matrices in the literature) summarize the known anatomical connectivity between pairs of regions of interest (RoIs) in the brain, regardless of whether they are active; sometimes published aCMs are binary and sometimes weighted by an approximate estimate of relative fiber density. In matrix notation RoIs are represented as nodes and the corresponding weights that connect these RoIs are represented as matrix entries. A symmetric aCM can be obtained using diffusion spectrum imaging or diffusion tensor imaging (DSI or DTI) that estimates weighted strengths of direct fiber links between brain regions, but does not record the direction of these links or whether they are active in any particular brain state. Symmetric functional connection matrices (fCMs) are most often determined from the covariance of activity in RoIs of the brain using functional magnetic resonance imaging (fMRI) (Friston, 2011; Bullmore and Sporns, 2009; Sporns, 2010; Aquino et al., 2012).

Several authors have tried to predict functional connectivity from anatomical connectivity and vice versa (Hagmann et al., 2008; Honey et al., 2009; Pernice et al., 2011; Goñi et al., 2014; Hutchison et al., 2011), but these early methods were mostly statistical, without an overarching physiologically based framework to deal with indirect, missing, and/or inactive connections. More recent estimates of the deCM used dynamic neural field and neural mass models to fit the fCM of a specific dynamic model to experiment (Gilson et al., 2016;

Deco et al., 2014). In their method, connectivity strengths were progressively adjusted until the best match with the resulting numerically calculated fCM was achieved; this work confirmed that near-criticality is required for a good match and that interhemispheric connections are underestimated, which is in accord with our earlier results that showed the brain functions in a near-critical state (Robinson et al., 1997, 2002; Robinson, 2012; Robinson et al., 2014). The CM that embodies the strengths of direct connections between points in a given brain state is termed a direct effective CM to unambiguously distinguish it from other types of effective CM (deCM, which has also previously been termed an effective CM or a gain matrix in the literature). Our recent work (Robinson et al., 2014) demonstrated how to identify the correctly normalized deCM from an experimental fCM via neural field theory (NFT) and eigenfunction analysis in the symmetric case. This was based on the method of Robinson (2012) to interrelate total effective CMs (teCMs, which measure all effects via both direct and indirect paths), deCMs, and fCMs. Meier et al. (2016) used the resulting power series expansion in further image analysis; however, this expansion has yet to be used to systematically investigate multistep (indirect) connections and their relative importance.

Here we address issues of estimating effective connectivity from the functional connectivity, including both direct and multistep connections, via the NFT propagator approach (Robinson, 2012). A *bare* neural field (NF) propagator represents only effects via direct connections with other regions of the network, and hence is identified with the deCM. A *dressed* propagator represents effects that travel via both direct and indirect connections and is thus identified with the teCM (Robinson, 2012; Robinson et al., 2014). Firstly, we present a method to estimate the deCM by minimizing the norm of the difference between an experimental fCM and the analytically calculated fCM for the aCM.

Secondly, we use these results to investigate underestimated connections in experimentally recorded aCMs. Thirdly, we explore the fact that the experimental fCM has fuller connectivity than the experimental aCM. Since DSI records direct connections only, we explore how various orders of multistep connections contribute to the observed activity (and hence the teCM and fCM) over and above the direct connectivity. This enables us to estimate the strengths of indirect connections via different numbers of intermediate RoIs and compare our result with experiment. Lastly, we present a method to analytically estimate the effective strengths of multistep connections vs. the number of steps.

2. Theory

Our work is based on NFT results that relate structure and functional connectivity (Robinson, 2012). In this section we briefly summarize the relevant aspects of NFT in propagator form, including how it interrelates effective and functional CMs.

2.1. Neural Field Theory and Propagator Approach to Connection Matrices

Our physiologically based NFT of brain dynamics incorporates arbitrary numbers of structures and neural populations (Robinson, 2005, 2012). These distinct neural populations are spatially distributed in the brain and their activity is influenced by neural inputs from various afferent populations.

The quantity $Q_a(\mathbf{r}, t)$ represents the spiking rate of a neural population a at position $\mathbf{r}$ at time t in the brain. An important point here is that Q_a can be used to represent either a mean firing rate or a perturbation from that mean. In the context of fMRI, experimental fCMs are constructed by calculating correlations or covariances of small differences from baseline activity (Friston, 2011; Bullmore and Sporns, 2009; Sporns, 2010; Honey et al., 2010). As discussed in detail elsewhere (Robinson, 2012; Robinson et al., 2014), we thus concentrate on

perturbations from baseline activity and restrict attention to the linear regime, noting that BOLD signal fluctuations are driven by local neural activity, primarily that of excitatory pyramidal cells (Attwell and Laughlin, 2001; Aquino et al., 2012).

Since spikes in population a are elicited by inputs from various afferent populations, which we label $b = 1, \ldots, p$, we can write

$$Q_a(\mathbf{r}, t) = \sum_b \int\int \tilde{\Lambda}_{ab}(\mathbf{r}, t, \mathbf{r}', t') Q_b(\mathbf{r}', t') d\mathbf{r}' dt' + N_a(\mathbf{r}, t), \qquad (1)$$

where the causal propagator $\tilde{\Lambda}_{ab}$ in Eq. (1) quantifies the effect of afferent activity in population b on population a, integrates over all sources locations $(\mathbf{r}', t')$, and $N_a(\mathbf{r}, t)$ is the external input (Robinson, 2012).

Equation (1) allows for temporal dynamics. To obtain the most commonly measured purely spatial deCM that measures influences of one point on another without regard to timing, one must integrate $\tilde{\Lambda}_{ab}$ over all possible values of t and t' to account for all influences that travel directly to $(\mathbf{r}, t)$ from $(\mathbf{r}', t')$, regardless of timing (Robinson et al., 1997; Knock et al., 2009). This yields the purely spatial propagator,

$$\tilde{\Lambda}(\mathbf{r}, \mathbf{r}') = \int\int \tilde{\Lambda}(\mathbf{r}, t, \mathbf{r}', t') dt dt', \qquad (2)$$

which remains implicitly causal. Because Eq. (1) is linear, it is possible to eliminate all but one of the Q_a from this set of equations and term it Q henceforth. Then if the brain is discretized into n regions, the quantities in the resulting equation can be collectively written in matrix notation as $\mathbf{Q}$, $\tilde{\mathbf{\Lambda}}$, and $\mathbf{N}$, where $\mathbf{Q}$ and $\mathbf{N}$ are n-element column matrices, $\tilde{\mathbf{\Lambda}}$ is $n \times n$, and any time dependence of $\tilde{\mathbf{\Lambda}}$ is ignored henceforth. The equation for $\mathbf{Q}$ can then be written in matrix

notation as (Honey et al., 2009)

$$\mathbf{Q} = \tilde{\mathbf{\Lambda}}\mathbf{Q} + \mathbf{N}. \quad (3)$$

From Eq. (3) one obtains the standard result for the response of a linear system to an external stimulus $\mathbf{N}$ (Robinson, 2012; Galán, 2008):

$$\mathbf{Q} = \left[\mathbf{I} - \tilde{\mathbf{\Lambda}}\right]^{-1}\mathbf{N}, \quad (4)$$

$$= \mathbf{T}\mathbf{N}, \quad (5)$$

$$= (\mathbf{I} + \mathbf{\Lambda})\mathbf{N}, \quad (6)$$

where $\mathbf{I}$ is the identity matrix and the superscript -1 denotes the matrix inverse. Equation (5) defines the transfer matrix $\mathbf{T}$ that relates the activity $\mathbf{Q}$ to an input $\mathbf{N}$. The matrix $\mathbf{\Lambda}$ is defined by Eq. (6) and is termed the total effective CM (teCM), which was referred to as the eCM and identified with the NFT dressed propagator by Robinson (2012). The teCM measures the total connectivity between RoIs via both direct and indirect paths. Expansion of Eq. (4) in a matrix power series shows that

$$\mathbf{\Lambda} = \tilde{\mathbf{\Lambda}} + \tilde{\mathbf{\Lambda}}^2 + \tilde{\mathbf{\Lambda}}^3 + \ldots + \tilde{\mathbf{\Lambda}}^m, \quad (7)$$

where this series converges provided all eigenvalues of $\tilde{\mathbf{\Lambda}}$ are of less than unit modulus, which is a sufficient condition for the network to be stable and thus able to exhibit normal brain activity (Robinson et al., 2014). The terms $\tilde{\mathbf{\Lambda}}^m$ correspond to propagation via $m-1$ intermediate RoIs, as shown in Fig. 1. Unlike statistical partial correlation methods (Zalesky et al., 2012), this explanation separates all levels of multistep connections and is based directly on the

physics of the system.

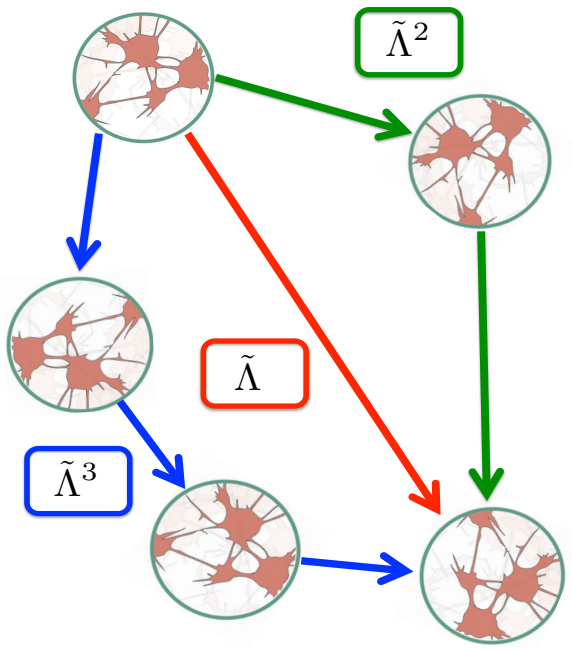

Figure 1: Connections between two RoIs: direct connections (red), connections via one intermediate RoI (green), and connections via two intermediate RoIs (blue). The box next to each path contains the corresponding term in the matrix representation of connectivity between two RoIs via, 0, 1, 2, ..., intermediate RoIs; i.e., $\tilde{\mathbf{\Lambda}}, \tilde{\mathbf{\Lambda}}^2, \tilde{\mathbf{\Lambda}}^3, \ldots$, respectively. The sum of all such terms is the total eCM (teCM, $\mathbf{\Lambda}$) or dressed propagator.

A quantity often used to define the fCM is the covariance matrix of activity at spatial locations $\mathbf{r}$ and $\mathbf{r}'$ (Friston, 2011; Bullmore and Sporns, 2009; Sporns, 2010; Honey et al., 2010),

$$\mathbf{C}(\mathbf{r}, \mathbf{r}') \quad = \quad \left\langle \mathbf{Q}(\mathbf{r}, t) \mathbf{Q}^T(\mathbf{r}', t) \right\rangle , \tag{8}$$

where the superscript T denotes the transpose of the matrix and angle brackets indicate an average over t, or equivalently if the system is ergodic, over real-

izations of the external inputs. If the inputs are white noise, Eq. (5) yields the matrix form (Robinson, 2012)

$$\mathbf{C} = \mathbf{T}\mathbf{T}^T. \tag{9}$$

Since $\mathbf{C}$ is symmetric, it contains no information on timing or the direction of causality between $\mathbf{r}$ and $\mathbf{r}'$. Usually, the covariance is normalized by dividing it by the variance when defining the fCM.

A further point that must be stressed is that the experimental fCM is often calculated after removal of the global brain signal to avoid artifacts from heartbeats, breathing, and head motion, that are common across the brain (Murphy et al., 2009; He and Liu, 2012). These signals are removed during experimental data processing. The experimental data discussed here, also removes any global neural signals and corresponding BOLD responses. Details of the global brain signal removal can be found in Hagmann et al. (2008). Hence, throughout the present work we remove the global spatially uniform mode, which corresponds to the lowest eigenmode of the theoretical deCM, before computing the covariance for comparison with the experimental fCM, which corresponds to subtracting from $\mathbf{C}$ the product of the activities in the global mode at the two points being correlated.

3. Methods

In this section we briefly introduce the experimental dataset used to illustrate the method. Based on the form Robinson (2012) NFT analysis mentioned in Sec. 2, we then present our method to obtain the deCM by fitting the calculated fCM to an experimentally recorded fCM, and explain the approach we use to investigate multistep connections. A number of new analytic results are derived here. We stress that the methods used in the present work do not require any

simulations of NFT whatsoever.

3.1. Experimental aCM, fCM, and distance between RoIs

To illustrate our method, throughout this paper we use a published experimental aCM that was obtained using DSI scans of the resting brains of five healthy right-handed male subjects, aged between 24 and 32 years (Hagmann et al., 2008). Other experimental datasets are available, but this widely used dataset has both aCM and fCM, with a large number of RoIs and it suffices to test our method. Hagmann et al. (2008) constructed a symmetric square aCM of size 998×998 with real positive entries using fiber tractography. The 998 nodes in the matrix cover the entire cortex, each defining an RoI. Each matrix entry is an undirected measure of the connection density of the fibers between two regions, averaged across the subjects (Hagmann et al., 2008).

In the experiment that produced the data we are using, a "resting state" fCM of same size was constructed using fMRI imaging of the same subjects (Honey et al., 2009). These authors computed time series for the same registered 998 ROIs as the aCM, the global component of the signal was removed (Hagmann et al., 2008), and covariances of the residual signals were computed to construct the 998×998 fCM (Honey et al., 2009).

The experimental aCM and fCM represent interhemispheric and intrahemispheric connectivity. The top left submatrix of size 500×500 represent connections within the right hemisphere and the bottom right submatrix of size 498×498 represents connections within the left hemisphere. The other two submatrices represent interhemispheric connections.

In the experimental data, 5 RoIs from the right hemisphere and 4 from the left hemisphere have no connections to any other RoIs. The RoIs that are not part of the connectivity network thus were deleted from the aCM and corresponding fCM. For the analysis in Sec. 3.2.1, individual CMs for the two

hemispheres of the same size are needed. We thus also delete the RoI in the right hemisphere that has the least connectivity with other RoIs, this step has negligible effect on the connectivity network in the experimental aCM. These steps give an experimental aCM ($\mathbf{aCM}_{\rm expt}$) of size 988 $\times$ 988 with each hemisphere of size 494 $\times$ 494, as shown in Fig. 2(a) with the corresponding experimental fCM ($\mathbf{fCM}_{\rm expt}$) in Fig. 2(b).

The experimental data include the Cartesian coordinates of the RoIs, from which we calculate the Euclidean distance between each pair.

3.2. Norm Minimization

The symmetric $\mathbf{aCM}_{\rm expt}$ from Sec. 3.1 records estimated anatomical connections between RoIs. However, the activity that underlines the fCM is supported by all active connections, whether or not their strengths are correctly estimated in $\mathbf{aCM}_{\rm expt}$. Our first approximation to calculate the fCM from the $\mathbf{aCM}_{\rm expt}$ is to assume that the deCM, $\tilde{\mathbf{\Lambda}}$, is linearly proportional to $\mathbf{aCM}_{\rm expt}$; i.e.,

$$\tilde{\mathbf{\Lambda}} \;=\; c\,\mathbf{aCM}_{\rm expt}, \tag{10}$$

where c is a constant to be determined. In the absence of data on directionality, it is natural to make this ansatz that the strength of connectivity in the approximated deCM is proportional to the connectivity strengths in the $\mathbf{aCM}_{\rm expt}$, which are proportional to the number of axons that connect the pairs of regions. Indeed, this is the most commonly used approximation in predictive studies (Knock et al., 2009; Deco et al., 2008; Alstott et al., 2009). However, we note that there is actually some asymmetry in the anatomical connectivity and this is neglected in approximation (Gilson et al., 2016; Sporns, 2010). The approximation in Eq. (10) also fails if significant number of connections are missed in $\mathbf{aCM}_{\rm expt}$, and/or if the relative strengths of different connections are

not well estimated in $\mathbf{aCM}_{\mathrm{expt}}$, points to which we return below.

We estimate c by using the NFT formula (9) to calculate the functional connection matrix ($\mathbf{fCM}_{\mathrm{cal}}$) as a function of c and then minimize $\delta(c)$, the fractional norm of the difference between $\mathbf{fCM}_{\mathrm{cal}}$ and the experimental matrix $\mathbf{fCM}_{\mathrm{expt}}$, with

$$\delta(c) \quad = \quad \frac{\|\mathbf{fCM}_{\mathrm{expt}} - \mathbf{fCM}_{\mathrm{cal}}(c)\|}{\|\mathbf{fCM}_{\mathrm{expt}}\|}, \tag{11}$$

where $\|\ldots\|$ denotes the Frobenius matrix norm defined as follows: for an $n \times n$ matrix S with elements s_{ij},

$$\|S\| \quad = \quad \left[\sum_{i,j=1}^{n} |s_{ij}|^2\right]^{1/2}. \tag{12}$$

Note that the $\|S\|$ is a standard measure of the size of a matrix S (Zhou and Doyle, 1998), which is zero if and only if $S = 0$.

3.2.1. Approximation of interhemispheric connections

A well known anatomical feature of the normal brain is the existence of strong one to one connections between homologous regions of the two hemispheres (Bullmore and Sporns, 2009; Sporns, 2010; Honey et al., 2009). However, these connections are underestimated in the $\mathbf{aCM}_{\mathrm{expt}}$ (Hagmann et al., 2008). Here we first approximate the effect of the missing connections by replacing the submatrices that correspond to interhemispheric connections by scaled identity matrices to represent connections between homologous regions in the $\mathbf{aCM}_{\mathrm{expt}}$; in a second approximation we use scaled versions of the intrahemispheric connections for this purpose. The approximations are further detailed in the following paragraph.

A general block representation of the $\mathbf{aCM}_{\mathrm{expt}}$ is

$$\mathbf{aCM}_{\mathrm{expt}} \quad = \quad \begin{pmatrix} \mathbf{A} & \mathbf{X} \\ \mathbf{X}^T & \mathbf{B} \end{pmatrix}, \tag{13}$$

where the submatrix $\mathbf{A}$ represents connections within the right hemisphere, the submatrix $\mathbf{B}$ represents ones within the left hemisphere, and the submatrix $\mathbf{X}$ represents interhemispheric connections from right to left hemisphere; because $\mathbf{aCM}_{\mathrm{expt}}$ is symmetric, the transposed submatrix $\mathbf{X}^T$ represents the connections from left to right hemisphere.

Many experiments underestimate the strengths of interhemispheric connections, and miss some altogether. However, anatomically it is known that the strongest interhemispheric connections exist between exactly homologous regions (Salvador et al., 2005; Kandel et al., 2000). Hence, to gain a better understanding of the role of the interhemispheric connections and their effects on the fCM, we thus first explore an approximation in which all possible connections between homologous regions are present and are assumed to have the same strength. In this approximation we replace $\mathbf{X}$ in Eq. (13) by $\mathbf{X}_{\mathrm{new}}$, with

$$\mathbf{X}_{\mathrm{new}} \quad = \quad a\mathbf{I}, \tag{14}$$

where $\mathbf{I}$ is the identity matrix of the same size of $\mathbf{X}$, and a is a small constant, which we later estimate by repeating the procedure discussed in Sec. 3.2, but minimizing the norm in Eq. (10) as a function of both c and a. In a second approximation we allow for the spatial spread of interhemispheric projections beyond exactly homologous locations by approximating the interhemispheric connectivity as a multiple of the mean intrahemispheric ones, and write

$$\mathbf{X}_{\mathrm{new}} \quad = \quad a(\mathbf{A}+\mathbf{B})/2. \tag{15}$$

3.3. Multistep connections

The experimental literature shows that fCMs have fuller connectivity than aCMs or deCMs (Honey et al., 2009; Hagmann et al., 2008; Honey et al., 2007) because aCMs and deCMs includes only direct connections, whereas the fCM incorporates effects from multistep (indirect) connections in addition to those of direct paths between RoIs, as discussed in Sec. 2 of the paper and by Robinson (2012) and Robinson et al. (2014). Figure 1 illustrates direct and indirect paths between RoIs.

For any square matrix $\mathbf{S}$ and a positive integer m, the ij element of $\mathbf{S}^m$ measures the total weighted connectivity due to all m-step paths to i from j (Fiedler, 2008). Hence, $\tilde{\mathbf{\Lambda}}^m$ describes connections that travel through $m-1$ intermediate RoIs to reach their destination. One summary measure of the relative contributions of multistep connections to the teCM $\mathbf{\Lambda}$ is thus obtained by calculating the matrix norms of the individual $\tilde{\mathbf{\Lambda}}^m$, as discussed after Eq.(12).

Neural field theory (NFT) has been shown to be able to approximate brain activity in a wide variety of situations, based on an approximate propagator that is the same at all points in the brain (Robinson et al., 1997; Robinson, 2012; Deco et al., 2008). The approximation of constant propagator structure across the brain is in accord with the approximate first-order uniformity of short to medium range connectivity found by many authors (Braitenberg and Schüz, 1998; Henderson and Robinson, 2011, 2013; Roberts et al., 2016). The NFT propagator expresses how brain activity is transmitted between points and its purely spatial version was identified with the deCM by Robinson (2012).

3.4. Analytical estimation of multistep connections

The spatial deCM that corresponds to NFT with Laplacian spatial coupling on the 2D cortical surface is (Robinson, 2012; Robinson et al., 1997) is of the

form

$$\tilde{\Lambda}(\mathbf{r},\mathbf{r}') = \tilde{\Lambda}(R) \quad = \quad \frac{K_0(R/r_{ee})}{2\pi r_{ee}^2}, \tag{16}$$

in coordinate notation, where r_{ee} is the characteristic range of excitatory fibers, $R = |\mathbf{R}|$, $\mathbf{R} = \mathbf{r} - \mathbf{r}'$, and K_0 is a modified Bessel function of the second kind; i.e., a Macdonald function (Abramowitz and Stegun, 1972). For notational simplicity, the spatial deCM, $\tilde{\Lambda}(R)$ is written as $\Lambda_1(R)$, where the subscript 1 denotes a direct one-step connection.

The spatial Fourier transform of a 2D function $F(\mathbf{R})$, and its inverse, are

$$F(\mathbf{k}) \quad = \quad \int e^{-i\mathbf{k}\cdot\mathbf{R}} F(\mathbf{R}) d^2\mathbf{R}, \tag{17}$$

$$F(\mathbf{R}) \quad = \quad \frac{1}{(2\pi)^2} \int e^{i\mathbf{k}\cdot\mathbf{R}} F(\mathbf{k}) d^2\mathbf{k}, \tag{18}$$

where $\mathbf{k}$ is the wavenumber. For a radially symmetric propagator, the Fourier transform and its inverse become

$$F(k) \quad = \quad 2\pi \int_0^\infty R\, F(R)\, J_0(kR)\, dR, \tag{19}$$

$$F(R) \quad = \quad \frac{1}{2\pi} \int_0^\infty k\, F(k)\, J_0(kR)\, dk, \tag{20}$$

where $J_0(kR)$ is the Bessel function of order zero. Applying Eq. (19) to Eq. (16), we find

$$\Lambda_1(k) \quad = \quad \frac{1}{r_{ee}^2} \int_0^\infty R\, K_0(R/r_{ee})\, J_0(kR)\, dR, \tag{21}$$

$$\quad = \quad \frac{1}{1 + k^2 r_{ee}^2}, \tag{22}$$

where Eq. 6.521.2 of Gradshteyn and Ryzhik (1980) has been used.

From anatomical studies it is observed that the connectivity across the cor-

tex is translationally invariant in space to a first approximation (Braitenberg and Schüz, 1998; Henderson and Robinson, 2013), and this has been described using NFT via a propagator approach (Robinson, 2012). A major advantage of the translationally invariant system is that the propagator is parametrized by coordinate differences, not by the coordinates themselves. The connectivity between two RoIs via one intermediate RoI is a two-step process in the spatial deCM, which can be written as

$$\Lambda_2(\mathbf{R}-\mathbf{R}') = \int d^2\mathbf{R}''\ \Lambda_1(\mathbf{R}-\mathbf{R}'')\Lambda_1(\mathbf{R}''-\mathbf{R}'), \quad (23)$$

$$= \{\Lambda_1 \otimes \Lambda_1\}(\mathbf{R}-\mathbf{R}'), \quad (24)$$

where $\mathbf{R}''$ is the intermediate position connecting $\mathbf{R}$ and $\mathbf{R}'$, and $\otimes$ denotes the convolution. This means that, for the space-invariant system, the two-step process is explained by the convolution of the propagator Λ_1 over all possible locations $\mathbf{R}''$ where the intermediate neurons could occur.

Using inverse Fourier transform of Eq. (23) we thus find

$$\Lambda_2(R) = \int_0^\infty k\ [\Lambda_1(k)]^2 J_0(kR)dk, \quad (25)$$

via the convolution theorem (Olver, 2010), which states

$$\{g \otimes h\}(k) = g(k)h(k). \quad (26)$$

Multiple iteration of the convolution theorem then implies

$$\Lambda_m = \underbrace{\Lambda_1 \otimes \Lambda_1 \otimes \ldots \otimes \Lambda_1}_{m}. \quad (27)$$

Hence, we find that the propagator for the m-step process is given by

$$\Lambda_m(R) \;=\; \frac{1}{2\pi}\int_0^\infty k\,[\Lambda_1(k)]^m J_0(kR)dk. \tag{28}$$

Using Eq. 2.12.4-28 of Prudnikov et al. (1998), the integral in Eq. (28) then yields our final results.

$$\Lambda_m(R) \;=\; \frac{1}{r_{ee}^2}\,\frac{K_{m-1}(R/r_{ee})}{2\pi(m-1)!}\left(\frac{R}{2r_{ee}}\right)^{m-1}. \tag{29}$$

Note that Λ_m depends only on the magnitude R of the distance between points and not on the direction of one relative to the other. Equation (29) enables us to analytically estimate the strength of connectivity between $\mathbf{r}$ and $\mathbf{r}'$ via $m-1$ intermediate RoIs. In later sections, we use the small-R limit of Eq. (28), which is (Olver, 2010).

$$\Lambda_1(R) \;\approx\; \frac{-\ln(R/2r_{ee})}{2\pi r_{ee}^2}, \tag{30}$$

$$\Lambda_m(R) \;\approx\; \frac{1}{4\pi r_{ee}^2(m-1)}, \tag{31}$$

where Eq. (31) applies for $m > 1$.

The total strength of connectivity X_m from a given point via $m-1$ intermediate nodes is a useful measure of multistep connectivity, with

$$X_m(R_{\max}) \;\approx\; 2\pi\int_0^{R_{\max}} R\Lambda_m(R)dR, \tag{32}$$

where $R_{\max}$ is the maximum range of fibers in the brain. A useful estimate of $R_{\max}$ is obtained by setting the area of a circle of radius $R_{\max}$ equal to the surface area S of one brain hemisphere. Since the data used in this manuscript was registered to the template brain "fsaverage" in FreeSurfer v5.3 (http://freesurfer.net) (Dale et al., 1999), S is calculated by taking the average surface area of the left

and right hemispheres which yields $S \approx 930$ cm^2 and $R_{\max} \approx 17$ cm, which almost identical to the longest ranges in the dataset discussed in Sec. 3.1.

The integral in Eq. (32) can be evaluated in the limit $R_{\max} \to \infty$ using Eq. 6.561.16 of Gradshteyn and Ryzhik (1980). This is a reasonable approximation if there are few fibers longer than the typical half-circumference of one brain hemisphere, which is in accord with anatomical and imaging experiments (Kandel et al., 2000; Wedeen et al., 2008; Hagmann et al., 2008, 2010). This gives,

$$X_m(\infty) \quad = \quad 1. \tag{33}$$

The interpretation of this result is that every m-step path ends up somewhere with unit probability; it generalizes the corresponding result of Robinson et al. (1997) for single-step propagation. When the brain is just below its critical point, only a fraction (eigenvalues $\tilde{\lambda}_1 < 1$) of activity is regenerated at each step of transmission through multiple intermediate nodes. Hence, the above $\mathbf{\Lambda}_m(R)$ must be multiplied by $\tilde{\lambda}_1^m$ to allow for this.

Experimental Estimate of Propagator vs. R

Equation (29) predicts the strength of connectivity between the spatial locations on the cortex as a function of their distance apart, R. In contrast, experimental connection matrices are expressed in terms of node number. To compare with the experimental data, the experimental connectivities are binned according to distances between nodes. The distance was calculated from the Cartesian coordinates, which are also available from the experiment (see Sec. 3.1). The results of average strength of connectivity $\overline{\mathbf{\Lambda}_m(R)}$ are then normalized so that the integral Eq. (32) satisfies $X_m = 1$ even in the finite brain. The same steps are followed to obtain the various experimental $\overline{\tilde{\mathbf{\Lambda}}^m(R)}$ from the corresponding $\tilde{\mathbf{\Lambda}}^m$. For n regions on the cortex, the quantities can be collectively written in

matrix notation as $\mathbf{\Lambda}_m(R)$ of size $n \times n$.

4. Results

In this section we first demonstrate results from the method described in Sec. 3.2 to estimate the deCM by fitting the calculated fCM to the experimental fCM, then compare the best match calculated fCM with the experimental fCM. Because the measured experimental aCM has underestimated interhemispheric connections, we also illustrate our method on a modified experimental aCM by replacing the interhemispheric connection submatrix by a scaled identity matrix to approximately represent all connections between homologous regions, described in Sec. 3.2.1. We then explore multistep connections using the methods of Sec. 3.3.

4.1. Best fit fCM and Inferred deCM

We use the norm-minimization method described in Sec. 3.2 to estimate the best fit fCM to the experimental fCM, and hence the corresponding deCM, for the experimental dataset described in Sec. 3.1. The difference between the experimental fCM ($\mathbf{fCM}_{\rm expt}$) and the calculated fCM ($\mathbf{fCM}_{\rm cal}(c)$) is shown by plotting the fractional difference $\delta(c)$ from Eq. (11) against c in Fig. 3, where c is the constant in Eq. (10). This involves minimization with respect to only one variable c, which is easily done by inspection of the of the graph $\delta(c)$ vs. c. The curve has a singularity at the critical point (beyond this point the system becomes linearly unstable) $c_{\rm cr} = 1.49$, where the largest eigenvalue $\tilde{\lambda}_1$ of the deCM estimated from Eq. (10) is 1 (Robinson, 2012); beyond this point the system is not linearly stable.

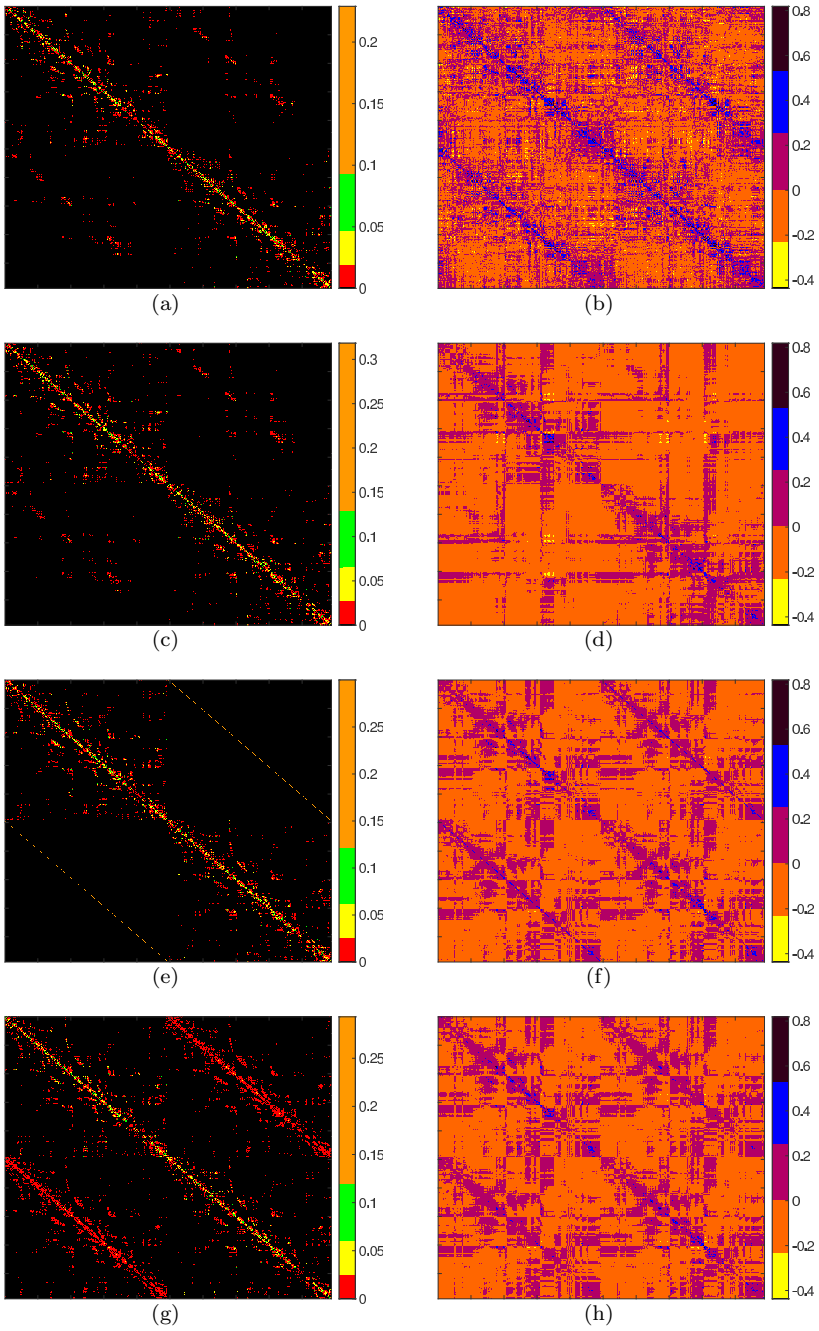

Figure 2: Comparisons between experimental and calculated CMs. (a) Experimental aCM from Hagmann et al. (2008). The top left submatrix represents the connectivity between RoIs in the right hemisphere and the bottom right represents the connectivity between RoIs in the left hemisphere. The other two submatrices represent interhemispheric connectivity. The matrix entries represent connectivity strengths, indicated by color. (b) Experimental fCM from (Hagmann et al., 2008; Honey et al., 2009). (c) Best fit inferred deCM for the experimental aCM in (a). (d) Best fit $\mathbf{fCM}_{\mathrm{cal}}$ calculated via norm minimization from Eq. (10). (e) Best fit deCM for the first approximation ($\mathbf{aCM}_{\mathrm{new}}$) in Eq. (14), where the interhemispheric connections (top right quadrant and bottom left quadrant of the experimental aCM) are replaced by the scaled identity matrix. (f) Best fit fCM calculated from the approximate deCM in (e). (g) Best fit deCM for the second approximation ($\mathbf{aCM}_{\mathrm{new}}$) in Eq. (15), where the submatrices corresponding to the interhemispheric connections (top right quadrant and bottom left quadrant of the experimental aCM) are replaced by the scaled intrahemispheric matrix. (h) Best fit fCM calculated from the deCM in (g).

The minimum fractional difference between fCMs $\delta_{\min}$ corresponds to $c_{\rm nrm} = 1.39$. At $c_{\rm nrm}$ the largest eigenvalue of the corresponding deCM, satisfies $\tilde{\lambda}_1 = c_{\rm nrm}/c_{\rm cr} = 0.93$, which implies that the brain is stable but near to the critical point in its normal functioning (Robinson et al., 1997, 2002, 2004; Gray and Robinson, 2009; Robinson et al., 2009, 2014); stability justifies linear analysis. Notably, the present estimate of the lowest mode's eigenvalue uses data which do not rely on this mode, owing to global mode removal; nonetheless, the result $c_{\rm nrm} = 0.93 c_{\rm cr}$ is remarkably consistent with previously published stability and criticality estimates from fCM inversion obtained by Robinson et al. (2014). Robinson et al. (2014) further discussed how their estimate was consistent with fits to various sets of EEG-based measurements (Rowe et al., 2004; Robinson et al., 2004; Van Albada et al., 2010), whose results implied $\tilde{\lambda}_1$ to have an average value of 0.85 ± 0.07 (Rowe et al., 2004), 0.84 ± 0.07 (Robinson et al., 2004), and 0.84 ± 0.05 (Van Albada et al., 2010), based on data from 100 to 1500 subjects. Other authors have also recently noted that the brain operates in a slightly subcritical state (Priesemann et al., 2014; Hansen et al., 2015).

Figure 2 shows results from our norm-minimization method. For the experimental dataset in Sec. 3.1, Fig. 2(a) shows $\mathbf{aCM}_{\rm expt}$. The top left submatrix represents the connectivity between RoIs in the right hemisphere and the bottom right represents the connectivity between RoIs in the left hemisphere. The other two submatrices represent interhemispheric connectivity. The primary diagonal and nearby entries show that RoIs are strongly connected to nearby regions via intrahemispheric connections. The secondary diagonals correspond to interhemispheric connections between homologous regions. These and nearby interhemispheric connections are seen to be only patchily detected in these data, as discussed in Sec. 3.1. The colorbar on the right indicate the strength of connectivity between RoIs, where black indicates absence of the connection.

Figure 2(b) shows the experimental fCM corresponding to the $\mathbf{aCM}_{\mathrm{expt}}$, with the same RoI ordering. We see that $\mathbf{fCM}_{\mathrm{expt}}$ is fuller than $\mathbf{aCM}_{\mathrm{expt}}$, with strong connectivity extending further away from the primary and secondary diagonals. It is noticeable that the connectivity pattern in the submatrix corresponding to the interhemispheric connections is similar to that of the submatrix corresponding to the intrahemispheric connections.

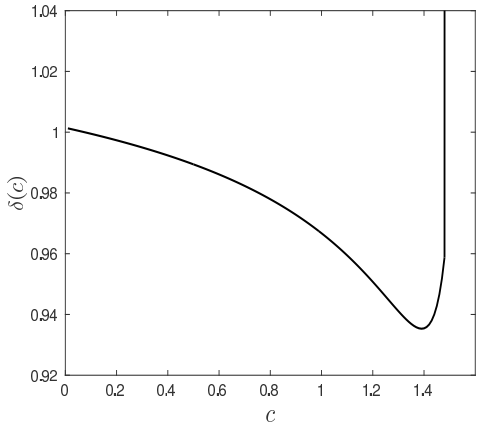

Figure 3: Fractional norm $\delta(c)$ of the difference between experimental and calculated fCMs vs. c from Eq. (11).

Figure 2(c) shows the deCM inferred on the assumption that it is a multiple of $\mathbf{aCM}_{\mathrm{expt}}$, estimated via norm minimization using the ansatz (10). Figure 2(d) shows the corresponding best fit calculated fCM inferred via norm minimization after removal of global effects; notably, it is *not* a multiple of the one in Fig. 2(b) because it has a different proximity to criticality (Robinson, 2012). The calculated fCM is the one that gives the best overall fit, as quantified by the norm. It reproduces the pattern of interhemispheric connections between RoIs near the primary diagonal reasonably well. However, the $\mathbf{fCM}_{\mathrm{cal}}$ has noticeably sparser connectivity in the submatrices that correspond to interhemispheric connections, particularly near the secondary diagonal. In contrast some rows and

columns have been enhanced along most of their length, because the detected on-diagonal interhemispheric connections in the aCM have been scaled up by our method to compensate for the underestimate of others when minimizing the overall norm.

If we replace the interhemispheric parts of the $\mathbf{aCM}_{\text{expt}}$ by scaled identity matrices to approximately account for underestimated connections, we can estimate a in Eq. (14) and c in (10) simultaneously via norm minimization. The contour plot of $\delta_{\min}$ vs. a and c in Fig. 4(a) shows that $\delta_{\min}$ occurs at $a = 0.116$ and $c = 1.31$. The corresponding deCM ($\mathbf{deCM}_{\text{new}}$) has largest eigenvalue $\tilde{\lambda}_1 = 0.93$, which is consistent with the largest eigenvalue found above. Figure 2(e) shows the deCM for the $\mathbf{aCM}_{\text{new}}$ estimated from this procedure. Figure 2(f) shows the corresponding fCM ($\mathbf{fCM}_{\text{new}}$) calculated from the deCM in Fig. 2(e) via norm minimization. The calculated $\mathbf{fCM}_{\text{new}}$ now shows a more uniform secondary diagonal that corresponds to interhemispheric connections, with less evidence of anomalously strengthened rows and columns. Notably, the calculated $\mathbf{fCM}_{\text{new}}$ has many entries that lie off the secondary diagonal, even though only the exact secondary diagonal was included in the approximate aCM. The range of connectivity strengths is consistent with those of the $\mathbf{fCM}_{\text{expt}}$, but the calculated $\mathbf{fCM}_{\text{new}}$ is not quite as full as the experimental one, likely due to the fact that no off-diagonal interhemispheric connections are included in the approximate aCM in Fig. 2(e).

Figure 2(g) shows the deCM for the $\mathbf{aCM}_{\text{new}}$ estimated by our second approximation of replacing the interhemispheric parts of the $\mathbf{aCM}_{\text{expt}}$ by scaled intrahemispheric matrices, as in Eq. (15). The parameters $a = 0.238$ and $c = 1.28$ were estimated using above procedure, as seen in Fig. 4(b). Figure 2(h) shows the fCM ($\mathbf{fCM}_{\text{new}}$) calculated from the deCM in Fig. 2(g) via norm minimization. The calculated $\mathbf{fCM}_{\text{new}}$ now shows a secondary diagonal that corresponds

to interhemispheric connections. As for Figs. 2(d) and 2(f), the range of connectivity strengths in the Fig. 2(h) is consistent with those of the $\mathbf{fCM}_{\mathrm{expt}}$, but the calculated $\mathbf{fCM}_{\mathrm{new}}$ is still visibly sparser than the experimental one.

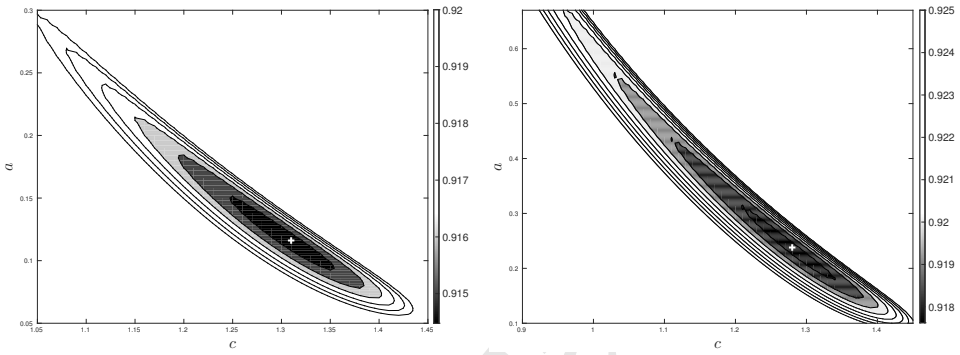

(a) (b)

Figure 4: Contour plot of $\delta_{\min}$ vs. a and c, with values indicated in the colorbar on the right. The value of a and c that correspond to minimum $\delta_{\min}$ is marked white. (a) estimates when the interhemispheric parts of the $\mathbf{aCM}_{\mathrm{expt}}$ is replaced by scaled identity matrices, in Eq. (14). (b) estimates when the interhemispheric parts of the $\mathbf{aCM}_{\mathrm{expt}}$ is replaced by scaled intrahemispheric matrices, in Eq. (15).

We note that both approximations in Eq. (14) and (15) implied connectivity strengths of $\mathbf{fCM}_{\mathrm{new}}$ consistent with those of the $\mathbf{fCM}_{\mathrm{expt}}$ and Figs. 2(f) and 2(h) confirm that experimental measurements underestimate interhemispheric connections. These approximations yield $\delta_{\min} = 0.915$ and 0.918, respectively, a negligible difference. However, in reality there do exist interhemispheric connections between non-homologous regions, so the approximation (15) in Fig. 2(g) is more appropriate. Hence, in the following sections we use the approximation Eq. (15).

4.2. Multistep connections

The fCM incorporates effects from multistep connections in addition to the direct path between RoIs, as discussed in Secs 2 and 3.3, but these cannot be

obtained directly from imaging experiments. This section presents results from analysis of direct and multistep connections, using the NFT described in Sec. 2 and the analytical approach described in Sec. 3.3. Here we present qualitative and quantitative results on connectivity in the brain with m-step connections and the contribution to functional activity based on the experimental dataset in Sec. 3.1.

The various multistep connections represented by the terms in right hand side of Eq. (7) are next investigated using $\mathbf{deCM}_{\text{new}}$ in Fig. 2(g). The first six terms are shown in Fig. 5 in matrix form for $m = 1 - 6$, estimated using the method in Sec. 3.3 with $\tilde{\lambda}_1 = 0.93$. The interhemispheric connection submatrices within $\tilde{\mathbf{\Lambda}}^m$ display prominent connections with regions of the opposite hemisphere other than those that are directly homologous. The interhemispheric connection submatrices are very similar in structure to the intrahemispheric submatrices. These results demonstrate the essential role of interhemispheric connections in determining the functional connectivity, which implies that their underestimation by many imaging techniques is an impediment to fully interrelating deCMs and fCMs.

We see from Fig. 5 that the connectivity tends to spread over the cortex as the number of intermediate nodes increases, with the matrices $\tilde{\mathbf{\Lambda}}^m$ showing fuller connectivity with increasing m. The experimental tractography technique is limited to measuring the strengths of direct connections ($m = 1$) between RoIs. Our NFT method enables us to estimate the strength of connections between RoIs via m-step connections. The matrix entries in $\tilde{\mathbf{\Lambda}}^m$ represent the strength of connections that travel m-step paths to reach their destination via $m - 1$ intermediate RoIs.

We next compare the experimental $\tilde{\mathbf{\Lambda}}^m$ with the theoretical $\mathbf{\Lambda}_m$ from Eq. (29). To do this we calculate the distance R between the RoIs using their Cartesian

coordinates from the original experiments (see Sec. 3.1). We then use the analytical definition of $\Lambda_m(R)$ in Eq. (29) to calculate the theoretical strength of connectivity for various m. The matrix representation of the first six terms is shown in Fig. 6, where we see that the connectivity spreads over the cortex as the number of intermediate nodes increases. These matrices are increasingly similar to the experimental ones in Fig. 5 as m increases.

The average strengths of experimental connectivity $\overline{\tilde{\mathbf{\Lambda}}^m(R)}$ vs. R are plotted in Fig. 7 for $m = 1, \ldots, 6$, normalized to total connectivity $X_m = 1$ in (32), along with the corresponding theoretical curves for $r_{ee} = 5.7$ mm, which gives the best fit at $R < 40$ mm for $m = 1$. At $R > 50$ mm there is a considerable excess of long-range fibers in the experimental case for $m = 1$ relative to extrapolation of the short-range theoretical approximation, a point that was discussed by Henderson and Robinson (2011). A more general theoretical prediction could be generated by including a dual-range distribution to account for these fibers, but we do not pursue this point here. For 10 mm $< R <$ 40 mm, the fit between theory and data is good and the value of $r_{ee} = 5.7$ mm is consistent with the value of 6.2 mm obtained by Henderson and Robinson (2013) for these data when fitted over a slightly different range. To avoid any confusion, the fact that there is an excess of long range fibers relative to simple extrapolation of the numbers of short range ones does not contradict the fact that interhemispheric fibers are often underestimated by diffusion imaging — the excess would be even greater if they were all detected.

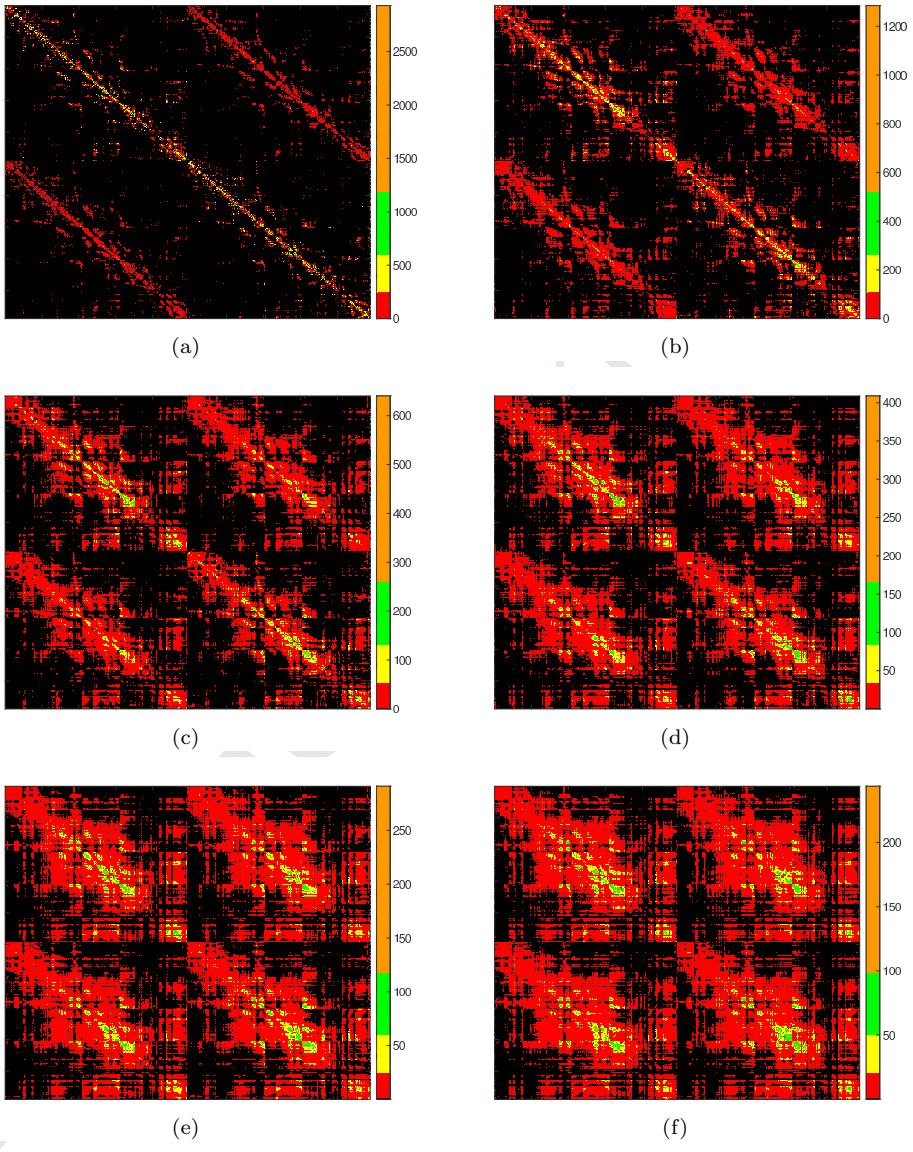

Figure 5: Matrix representations of the first six eCM terms of Eq. (7), calculated for the $\mathbf{aCM}_{\mathrm{new}}$ using second approximation in Eq. (15). (a) show direct connectivity of RoIs, $\tilde{\mathbf{\Lambda}}^1$, (b) two-step connectivity via 1 intermediate RoI, $\tilde{\mathbf{\Lambda}}^2$, (c) $\tilde{\mathbf{\Lambda}}^3$, (d) $\tilde{\mathbf{\Lambda}}^4$, (e) $\tilde{\mathbf{\Lambda}}^5$ and (f) $\tilde{\mathbf{\Lambda}}^6$. The colors indicate strength of connectivity per unit area.

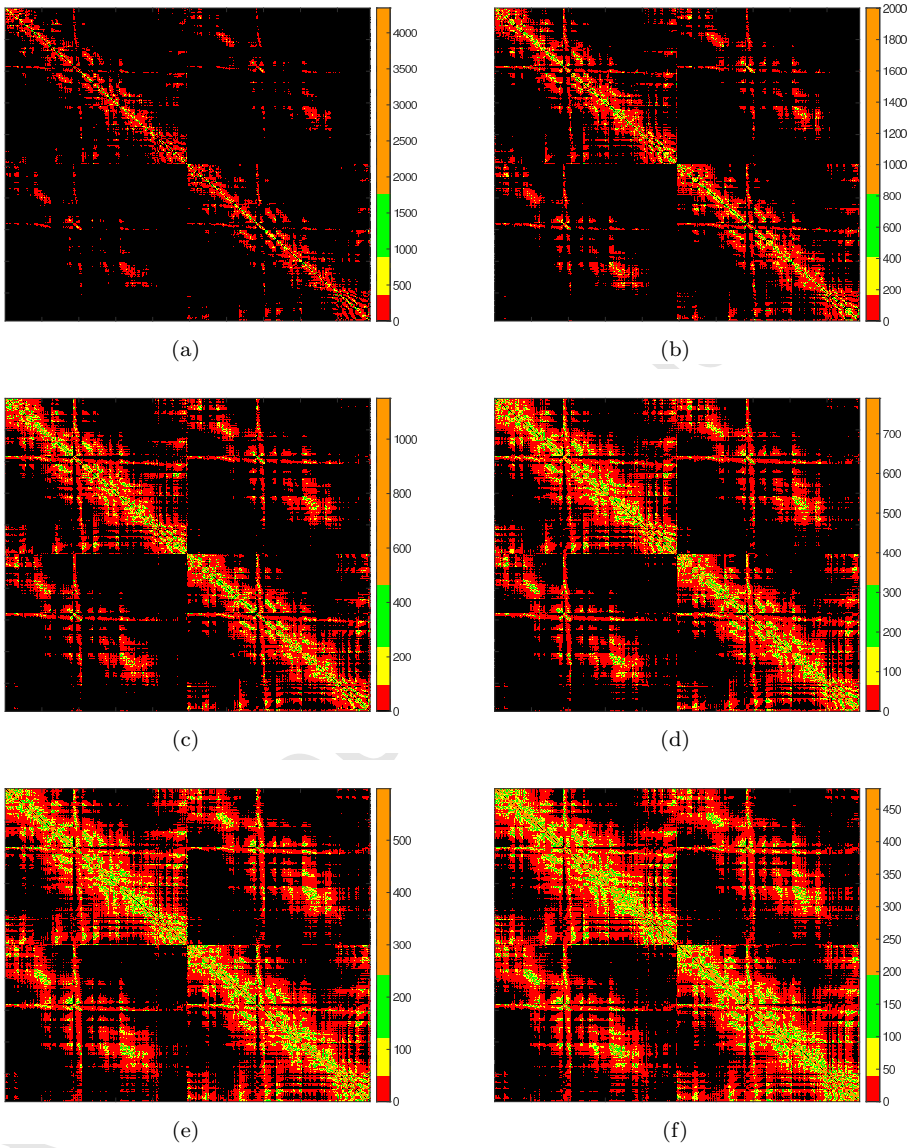

Figure 6: Theoretical estimates of the first six terms of the teCM from Eq. (29). Matrix entries represent the strength of connections per unit area as indicated in the color bar. (a) The inferred deCM $\mathbf{\Lambda}_1$, shows connectivity of RoIs with $m = 1$, (b) $\mathbf{\Lambda}_2$, (c) $\mathbf{\Lambda}_3$, (d) $\mathbf{\Lambda}_4$, (e) $\mathbf{\Lambda}_5$ and (f) $\mathbf{\Lambda}_6$.

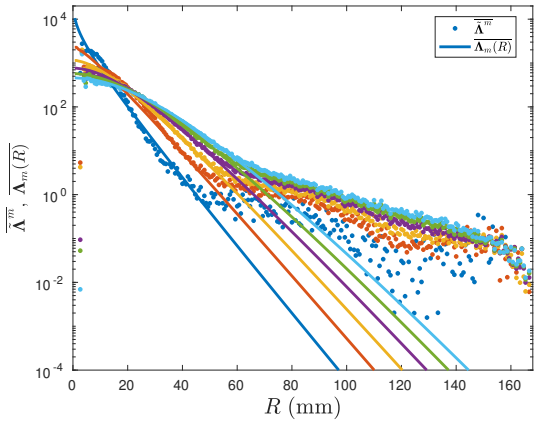

(a)

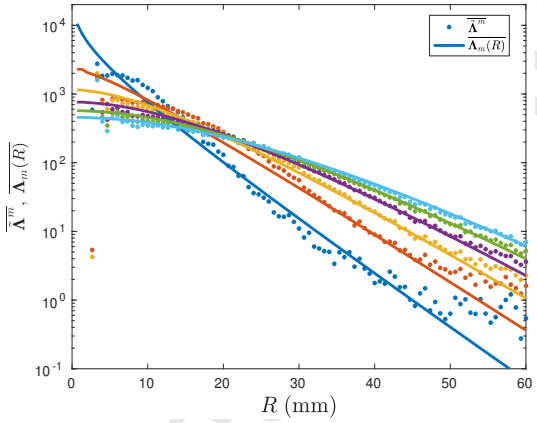

(b)

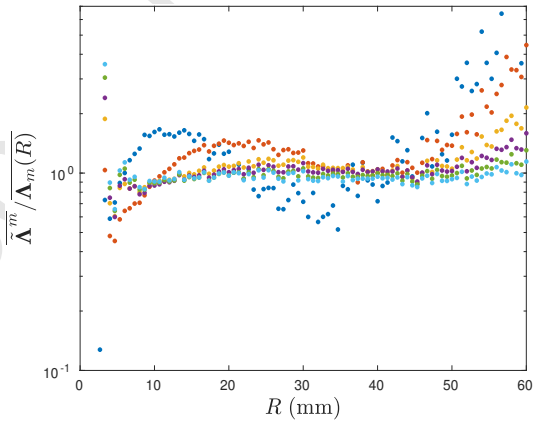

(c)

Figure 7: Comparison of the analytically estimated strength of connectivity per unit area with the experimental measurements for $m = 1$ (blue), $m = 2$ (red), $m = 3$ (yellow), $m = 4$ (purple), $m = 5$ (green), $m = 6$ (cyan). Dots represent experimental data and solid lines represent the analytical expression (29) for $r_{ee} = 5.7$ mm. (a) Average connectivity strength vs. R. (b) Zoom of (a) to focus on results up to $R = 60$ mm. (c) Ratios of experimental to analytical values from (b).

At $R < 10$ mm, we see that the theoretical curve for $m = 1$ lies systematically above the experimental one, as seen most clearly in the zoom in Fig. 7(b). This is expected because the theoretical result does not incorporate a resolution limit, whereas the typical RoI in these data has an area of 2 cm^2, which corresponds to a typical radius of 8 mm; because self-connections were omitted from the experimental CMs, the value of $\tilde{\mathbf{\Lambda}}^1(R)$ is expected to have been underestimated over roughly this range (and some RoIs are larger, so the effects extend somewhat beyond 8 mm), with no connections below the ~ 2 mm resolution of the measurements, as seen in the figure. In the range $10 - 40$ mm the theoretical and experimental curves agree remarkably well in terms of both magnitude and slope. We see that the connectivity spreads to larger R as m increases, with progressively weaker connectivity at relatively small R.

Figure 7(c) shows ratios of the experimental data in Fig. 7(b) to the theoretical ones. This underlines the near-unit ratio on average for all m over distances $10 - 40$ mm, with the ratios more nearly constant for larger m.

4.3. Connectivity From a Seed Voxel

A common way of exploring brain connectivity is to map the connections that emerge from a particular seed voxel. As an illustration, we show this in Fig. 8 for m-step connections for various m, starting with an arbitrarily chosen seed voxel that happens to lie in the left precuneus (PCUN) and using the $\mathbf{deCM}_{\rm new}$ shown in Fig. 5(a). We see that the connections rapidly extend across the cortex, with contrahemispheric connections lagging about one step behind those in the ipsilateral hemisphere, as expected from the necessity to have one interhemispheric connection in addition to any subsequent intrahemispheric ones in the contralateral case. Connectivity becomes increasingly uniform across the brain, but the short-range connections remain dominant even at $m = 12$. Notably, the magnitude of the largest connections decreases steadily with m.

Qualitatively, very similar results are found for other seed locations.

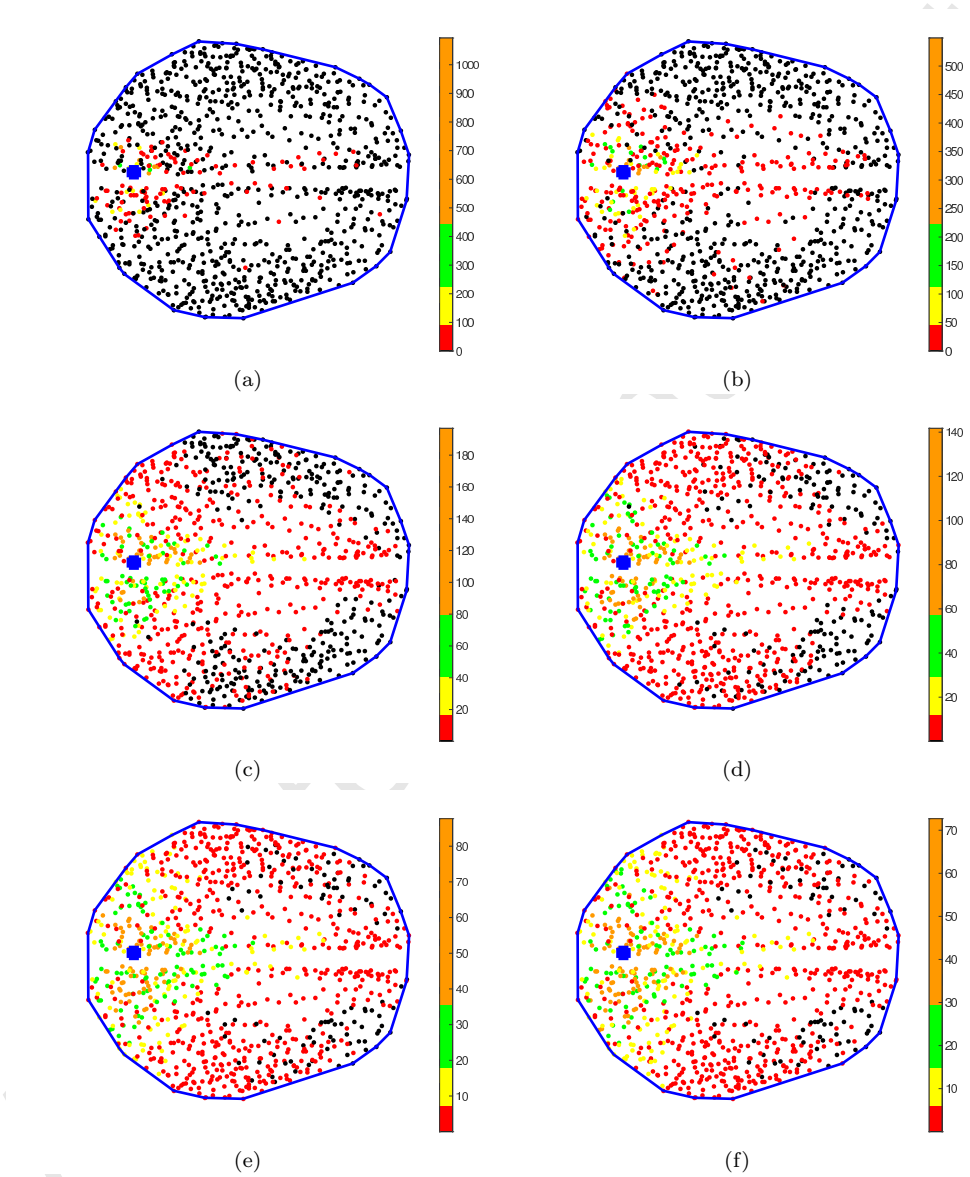

Figure 8: Connectivity from the seed voxel via m-step. Top view of the brain, plotted using the same coordinate system as the experimental data. A node (blue marker) from the precuneus (PCUN) is chosen to illustrate the anatomical connectivity strength with other RoIs of the brain. The dots represent location of RoIs on the brain. The blue marker represents the location of the precuneus. The color of each dot represents the strength of connectivity from PCUN, as indicated by the color bars. (a) $m = 1$. (b) $m = 2$. (c) $m = 4$. (d) $m = 6$. (e) $m = 10$. (f) $m = 12$.

5. Summary and Discussion

Neural field theory relationships between effective and functional connectivity matrices are used to develop a simple approximate norm-minimization method for obtaining direct effective connection matrices (deCMs) from functional CMs. Comparison with experimental results shows that this gives reasonable results so along as interhemispheric connections are adequately incorporated. Multistep connection matrices, obtained from powers of the deCM, are shown to be well represented by neural field theory, and to provide a powerful way of analyzing multistep connectivity in the brain. The main results are:

(i) By using the ansatz that the deCM is proportional to the aCM, we calculated the corresponding fCM based on methods from Robinson (2012). By minimizing the norm of the difference between this fCM and an experimentally measured one, we optimized the scaling factor, and thereby infer the normalized deCM.

(ii) When applied to test data from the literature, norm minimization yielded a best fit that corresponds to the cortex least stable mode being at approximately 93% of the critical value for a saddle node bifurcation into instability. Despite this estimate not relying on data from the last stable mode itself, it is consistent with prior quantitative estimates (Rowe et al., 2004; Robinson et al., 2004; Van Albada et al., 2010; Roberts et al., 2016), with conclusions from a model system (Deco et al., 2014), and with more recent studies that confirmed these earlier conclusions that the brain operates in a slightly subcritical state (Priesemann et al., 2014; Hansen et al., 2015). However, interhemispheric connections are underestimated where they are absent or underestimated in the initial aCM, leading to overemphasis of those that remain and resulting in anomalous patterns in the derived fCM.

(iii) After introducing connections between exactly homologous regions in

opposite hemispheres as an ansatz to replace underestimated ones (Robinson et al., 2016), norm minimization yields a much better match between predicted and experimental fCMs, with minimal anomalous structure. The system is estimated to lie at 93% of the critical point.

The filling factor of the predicted fCM is slightly less than the experimental one, because only exactly homologous connections between hemispheres are included in the deCM; nonetheless, the resulting fCM does include substantial nonhomologous entries. The conclusion that interhemispheric connections are critical to determining the structure of the fCM accords with those of other recent publications, based on inversion via eigenfunction analysis (Robinson et al., 2014) and by means of addition and fitting of entries in the aCM (Deco et al., 2014) within a specific neural field model. Notably, Robinson (2012) showed that fCMs with structure qualitatively consistent with observation only emerge near criticality.

(iv) When the interhemispheric connection matrices are approximated as being proportional to the intrahemispheric ones, norm minimization yields a much better match between predicted and experimental fCMs and the system is again estimated to lie at 93% of the critical point.

(v) The approximate deCMs obtained by the above method are correctly normalized in an absolute sense (Robinson, 2012). Hence, powers of this matrix give the relative patterns and strengths of multistep connections. These spread progressively as the number of intermediate RoIs increases, with spreading from a seed voxel lagging roughly one step in the contralateral hemisphere compared to the ipsilateral one.

(vi) deCMs estimated by our methods are very similar in form to the theoretical ones derived from neural field theory, aside from a normalization factor and effects due to the long-range tails neglected in the analytic work here (although

they can be included at the cost of additional algebraic complexity). This result further confirms recent conclusions that cortical connectivity is dominated by a uniform isotropic component that does not contain first-order modularity or hierarchy beyond what is implicit in the decrease of average connection strength with distance (Henderson and Robinson, 2011, 2013, 2014). To the extent that modularity, hierarchy, and nonuniformity are present in the cortex, they do not dominate leading-order statistics and result in part from the less uniform properties of the large-R tail of the connectivity distribution (Henderson and Robinson, 2014). Recently, departures from the uniformity approximation have been reliably detected for the first time (Roberts et al., 2016).

Overall, the method presented here enables simple approximate inversion of fCMs to obtain normalized deCMs, provided the form of the interhemispheric connections is included to a reasonable approximation. This is of great utility because it does not rely on a particular model of the system dynamics at the network nodes and yields estimates of effective connectivities that are difficult or impossible to measure experimentally.

6. Acknowledgments

We thank J. D. Griffths for helpful discussions, and Romesh G. Abeysuriya and John H. C. Palmer for comments on the manuscript. This work was supported by the Australian Research Council Center of Excellence for Integrative Brain Function (ARC Grant CE 140100007), ARC Laureate Fellowship Grant FL1401000225, ARC Federation Fellowship Grant FF0883155, and ARC Discovery Project Grant 130100437.

References

Abramowitz, M., Stegun, I.A., 1972. Handbook of Mathematical Functions. Dover, New York.

Albert, R., Barabási, A.L., 2002. Statistical mechanics of complex networks. Rev. Mod. Phys. 74, 47.

Alstott, J., Breakspear, M., Hagmann, P., Cammoun, L., Sporns, O., 2009. Modeling the impact of lesions in the human brain. PLoS Comput. Biol. 5, e1000408.

Aquino, K.M., Schira, M.M., Robinson, P., Drysdale, P.M., Breakspear, M., 2012. Hemodynamic traveling waves in human visual cortex. PLoS Comput. Biol. 8, e1002435.

Attwell, D., Laughlin, S.B., 2001. An energy budget for signaling in the grey matter of the brain. J. Cereb. Blood Flow Metab. 21, 1133–1145.

Barthélemy, M., 2011. Spatial networks. Phys. Rep. 499, 1–101.

Bassett, D.S., Meyer-Lindenberg, A., Achard, S., Duke, T., Bullmore, E., 2006. Adaptive reconfiguration of fractal small-world human brain functional networks. Proc. Natl. Acad. Sci. U.S.A. 103, 19518–19523.

Beggs, J.M., Plenz, D., 2003. Neuronal avalanches in neocortical circuits. J. Neurosci. 23, 11167–11177.

Braitenberg, V., Schüz, A., 1998. Cortex: Statistics and geometry of neuronal connectivity. 2nd ed., Springer, Berlin.

Bullmore, E., Sporns, O., 2009. Complex brain networks: graph theoretical analysis of structural and functional systems. Nat. Rev. Neurosci. 10, 186 – 198.

Dale, A.M., Fischl, B., Sereno, M.I., 1999. Cortical surface-based analysis: I. segmentation and surface reconstruction. NeuroImage 9, 179–194.

Damoiseaux, J., Rombouts, S., Barkhof, F., Scheltens, P., Stam, C., Smith, S.M., Beckmann, C., 2006. Consistent resting-state networks across healthy subjects. Proceedings of the national academy of sciences 103, 13848–13853.

Deco, G., Jirsa, V.K., Robinson, Peter A. Breakspear, M., Friston, K., 2008. The dynamic brain: From spiking neurons to neural masses and cortifields. PLoS Comput. Biol. 4, e1000092.

Deco, G., McIntosh, A.R., Shen, K., Hutchison, R.M., Menon, R.S., Everling, S., Hagmann, P., Jirsa, V.K., 2014. Identification of optimal structural connectivity using functional connectivity and neural modeling. J. Neurosci. 34, 7910–7916.

Fiedler, M., 2008. Special matrices and their applications in numerical mathematics. Courier Corporation,, New York.

Friston, K.J., 2011. Functional and effective connectivity: A review. Brain Connect. 1, 13–36.

Galán, R.F., 2008. On how network architecture determines the dominant patterns of spontaneous neural activity. PLoS One 3, e2148.

Gilson, M., Moreno-Bote, R., Ponce-Alvarez, A., Ritter, P., Deco, G., 2016. Estimation of directed effective connectivity from fmri functional connectivity hints at asymmetries of cortical connectome. PLoS Comput. Biol. 12, e1004762.

Goñi, J., Van Den Heuvel, M.P., Avena-Koenigsberger, A., de Mendizabal, N.V., Betzel, R.F., Griffa, A., Hagmann, P., Corominas-Murtra, B., Thiran, J.P., Sporns, O., 2014. Resting-brain functional connectivity predicted by analytic measures of network communication. Proc. Natl. Acad. Sci. U.S.A. 111, 833–838.

Gradshteyn, I., Ryzhik, I., 1980. Table of integrals, series and products, corrected and enlarged edition, 1980. Academic Press, New York.

Gray, R., Fung, C., Robinson, P., 2009. Stability of small-world networks of neural populations. Neurocomputing 72, 1565–1574.

Gray, R.T., Robinson, P.A., 2009. Stability and structural constraints of random brain networks with excitatory and inhibitory neural populations. J. Comput. Neurosci. 27, 81–101.

Hagmann, P., Cammoun, L., Gigandet, X., Meuli, R., Honey, C.J., Wedeen, V.J., Sporns, O., 2008. Mapping the structural core of human cerebral cortex. PLoS Biol. 6, e159.

Hagmann, P., Sporns, O., Madan, N., Cammoun, L., Pienaar, R., Wedeen, V.J., Meuli, R., Thiran, J.P., Grant, P., 2010. White matter maturation reshapes structural connectivity in the late developing human brain. Proceedings of the National Academy of Sciences 107, 19067–19072.

Hansen, E.C., Battaglia, D., Spiegler, A., Deco, G., Jirsa, V.K., 2015. Functional connectivity dynamics: modeling the switching behavior of the resting state. NeuroImage 105, 525–535.

He, H., Liu, T.T., 2012. A geometric view of global signal confounds in resting-state functional mri. NeuroImage 59, 2339–2348.

Henderson, J.A., Robinson, P.A., 2011. Geometric effects on complex network structure in the cortex. Phys. Rev. Lett. 107, 018102.

Henderson, J.A., Robinson, P.A., 2013. Using geometry to uncover relationships between isotropy, homogeneity, and modularity in cortical connectivity. Brain Connect 3, 423–437.

Henderson, J.A., Robinson, P.A., 2014. Relations between the geometry of cortical gyrification and white-matter network architecture. Brain Connect. 4, 112–130.

Honey, C.J., Kötter, R., Breakspear, M., Sporns, O., 2007. Network structure of cerebral cortex shapes functional connectivity on multiple time scales. Proc. Natl. Acad. Sci. U.S.A. 104, 10240–10245.

Honey, C.J., Sporns, O., Cammoun, L., Gigandet, X., Thiran, J.P., Meuli, R., Hagmann, P., 2009. Predicting human resting-state functional connectivity from structural connectivity. Proc. Natl. Acad. Sci. U.S.A. 106, 2035–2040.

Honey, C.J., Thivierge, J.P., Sporns, O., 2010. Can structure predict function in the human brain? NeuroImage 52, 766–776.

Hutchison, R.M., Womelsdorf, T., Gati, J.S., Leung, L.S., Menon, R.S., Everling, S., 2011. Resting-state connectivity identifies distinct functional networks in macaque cingulate cortex. Cereb. Cortex 22, 1294–308.

Kaiser, M., Hilgetag, C.C., Kötter, R., 2010. Hierarchy and dynamics of neural networks. Front. Neuroinform. 4, 112.

Kandel, E.R., Schwartz, J.H., Jessell, T.M., Siegelbaum, S.A., Hudspeth, A., 2000. Principles of neural science. volume 4. McGraw-hill New York.

Kitzbichler, M.G., Smith, M.L., Christensen, S.R., Bullmore, E., 2009. Broadband criticality of human brain network synchronization. PLoS Comput. Biol. 5, e1000314.

Knock, S., McIntosh, A., Sporns, O., Kötter, R., Hagmann, P., Jirsa, V., 2009. The effects of physiologically plausible connectivity structure on local and global dynamics in large scale brain models. J. Neurosci. Methods 183, 86–94.

Linkenkaer-Hansen, K., Nikouline, V.V., Palva, J.M., Ilmoniemi, R.J., 2001. Long-range temporal correlations and scaling behavior in human brain oscillations. J. Neurosci. 21, 1370–1377.

Meier, J., Tewarie, P., Hillebrand, A., Douw, L., Van Dijk, B.W., Stufflebeam, S.M., Van Mieghem, P., 2016. A mapping between structural and functional brain networks. Brain Connect. 6, 298–311.

Murphy, K., Birn, R.M., Handwerker, D.A., Jones, T.B., Bandettini, P.A., 2009. The impact of global signal regression on resting state correlations: are anti-correlated networks introduced? NeuroImage 44, 893–905.

Olver, F.W., 2010. NIST Handbook of Mathematical Functions. Cambridge University Press, New York.

Pernice, V., Staude, B., Cardanobile, S., RottStefan, 2011. How structure determines correlations in neuronal networks. PLoS Comput. Biol. 7, e1002059.

Priesemann, V., Wibral, M., Valderrama, M., Pröpper, R., Le Van Quyen, M., Geisel, T., Triesch, J., Nikolic, D., Munk, M.H., 2014. Spike avalanches in vivo suggest a driven, slightly subcritical brain state. Front. Syst. Neurosci. 8, 108.

Prudnikov, A.P., Brychkov, I.A., Marichev, O.I., 1998. Integrals and series: special functions. volume 2. Gordon and Breach, New York.

Roberts, J.A., Perry, A., Lord, A.R., Roberts, G., Mitchell, P.B., Smith, R.E., Calamante, F., Breakspear, M., 2016. The contribution of geometry to the human connectome. NeuroImage 124, 379–393.

Robinson, P., Zhao, X., Aquino, K., Griffiths, J., Sarkar, S., Mehta-Pandejee, G., 2016. Eigenmodes of brain activity: Neural field theory predictions and comparison with experiment. NeuroImage 142, 79–98.

Robinson, P.A., 2005. Propagator theory of brain dynamics. Phys. Rev. E 72, 011904.

Robinson, P.A., 2012. Interrelating anatomical, effective, and functional brain connectivity using propagators and neural field theory. Phys. Rev. E 85, 011912.

Robinson, P.A., Henderson, J.A., Matar, E., Riley, P., Gray, R.T., 2009. Dynamical reconnection and stability constraints on cortical network architecture. Phys. Rev. Lett. 103, 108104.

Robinson, P.A., Rennie, C.J., Rowe, D.L., 2002. Dynamics of large-scale brain activity in normal arousal states and epileptic seizures. Phys. Rev. E 65, 041924.

Robinson, P.A., Rennie, C.J., Rowe, D.L., O'Connor, S.C., 2004. Estimation of multiscale neurophysiologic parameters by electroencephalographic means. Hum. Brain. Mapp. 23, 53–72.

Robinson, P.A., Rennie, C.J., Wright, J.J., 1997. Propagation and stability of waves of electrical activity in the cerebral cortex. Phys. Rev. E 56, 826.

Robinson, P.A., Sarkar, S., Pandejee, G.M., Henderson, J.A., 2014. Determination of effective brain connectivity from functional connectivity with application to resting state connectivities. Phys. Rev. E 90, 012707.

Rowe, D.L., Robinson, P.A., Rennie, C.J., 2004. Estimation of neurophysiological parameters from the waking EEG using a biophysical model of brain dynamics. J. Theor. Biol. 231, 413–433.

Rubinov, M., Sporns, O., Thivierge, J.P., Breakspear, M., 2011. Neurobiologically realistic determinants of self-organized criticality in networks of spiking neurons. PLoS Comput. Biol. 7, e1002038.

Rubinov, M., Sporns, O., Van Leeuwen, C., Breakspear, M., 2009. Symbiotic relationship between brain structure and dynamics. BMC Neurosci. 10, 55.

Salvador, R., Suckling, J., Coleman, M.R., Pickard, J.D., Menon, D., Bullmore, E., 2005. Neurophysiological architecture of functional magnetic resonance images of human brain. Cerebral cortex 15, 1332–1342.

Sporns, O., 2010. Networks of the Brain. MIT Press, Cambridge.

Sporns, O., Chialvo, D.R., Kaiser, M., Hilgetag, C.C., 2004. Organization, development and function of complex brain networks. Trends Cogn. Sci. 8, 418–425.

Sporns, O., Tononi, G., Edelman, G., 2000. Theoretical neuroanatomy: Relating anatomical and functional connectivity in graphs and cortical connection matrices. Cereb. Cortex 10, 127–141.

Sporns, O., Tononi, G., Kötter, R., 2005. The human connectome: a structural description of the human brain. PLoS Comput. Biol. 1, e42.

Stam, C.J., de Bruin, E.A., 2004. Scale-free dynamics of global functional connectivity in the human brain. Hum. Brain. Mapp. 22, 97–109.

Van Albada, S.J., Kerr, C.C., Chiang, A.K.I., Rennie, C.J., Robinson, P.A., 2010. Neurophysiological changes with age probed by inverse modeling of EEG spectra. Clin. Neurophysiol. 121, 21–38.

Wedeen, V.J., Wang, R., Schmahmann, J.D., Benner, T., Tseng, W., Dai, G., Pandya, D., Hagmann, P., D'Arceuil, H., de Crespigny, A.J., 2008. Diffusion spectrum magnetic resonance imaging (dsi) tractography of crossing fibers. Neuroimage 41, 1267–1277.

Zalesky, A., Fornito, A., Bullmore, E., 2012. On the use of correlation as a measure of network connectivity. NeuroImage 60, 2096–2106.

Zhou, K., Doyle, J.C., 1998. Essentials of robust control. volume 104. Prentice hall Upper Saddle River, New Jersey.